

Multiscale Numerical Modelling of Ultrafast Laser–Matter Interactions: Maxwell–Two-Temperature Model–Molecular Dynamics (M-TTM-MD)

O. Benhayoun^{1,*} and M. E. Garcia¹

¹*Institute of Theoretical Physics II and Center for Interdisciplinary Nanostructure Science and Technology (CINSaT), Universität Kassel, Heinrich-Plett-Straße 40, 34132 Kassel, Germany*

(Dated: January 29, 2026)

Abstract

In this work, we present a comprehensive numerical framework that couples numerical solutions of Maxwell’s equations using the Finite-Difference Time-Domain (FDTD) approach, Molecular Dynamics (MD), and the Two-Temperature Model (TTM) to describe ultrafast laser–matter interactions in metallic systems at the atomic scale. The proposed Maxwell-Two-Temperature Model–Molecular Dynamics (M-TTM-MD) bridges the gap between electromagnetic field propagation, electron–phonon energy exchange, and atomic motion, allowing for a self-consistent treatment of energy absorption, transport, and structural response within a unified simulation environment. The calculated electromagnetic fields incorporate dispersive dielectric properties derived using the Auxiliary Differential Equation (ADE) technique, while the electronic and lattice subsystems are dynamically coupled through spatially and temporally resolved energy exchange terms. The changes in the material topography are then reflected in the updated grid for the FDTD scheme. The developed M-TTM-MD model provides a self-consistent numerical framework that offers insights into laser-induced phenomena in metals, including energy transport and surface dynamics under extreme nonequilibrium conditions.

Keywords: Multiscale Numerical Modelling, Ultrashort Laser–matter interactions, Molecular Dynamics, Two-Temperature Model, Finite-Difference Time-Domain

* obenayoun@uni-kassel.de

I. INTRODUCTION

Ultrafast laser–matter interaction has emerged as a key research area for understanding and controlling physical processes on femtosecond timescales. When a femtosecond laser pulse irradiates a metallic target, the absorbed energy is first deposited into the electronic subsystem, leading to a rapid increase of its temperature while the lattice remains at room temperature. The energy is then transferred to the ions via electron–phonon coupling, such that both systems eventually reach thermal equilibrium. This nonequilibrium process can be crucial for a wide range of ultrafast phenomena that require ablation or surface modification of the target material. One important application is the formation of Laser-Induced Periodic Surface Structures (LIPSS), in which periodic and uniform ripples can be formed at the surface of a wide variety of materials, ranging from dielectrics to metals [1–10].

To describe these dynamics, the Two-Temperature Model (TTM) [11, 12] has been widely employed, providing a macroscopic picture of the coupled electron and lattice temperature evolution. However, this approach lacks atomistic resolution and cannot capture local structural transformations. Molecular Dynamics (MD) simulations, on the other hand, offer atomic-scale insight into the lattice response but generally rely on empirical or uniform heating schemes that neglect spatially varying energy absorption and electromagnetic effects.

To address these limitations, more recent studies have coupled MD with the TTM formalism [13–15], yielding a more realistic description of lattice dynamics and phase transitions. However, most implementations still use simplified optical source terms and assume spatially uniform energy deposition, thereby overlooking electromagnetic-field evolution and material dispersion. Surface topography, for example, scatters the incident laser and can excite surface waves such as surface plasmon polaritons [2, 8, 10, 16], which significantly affect energy absorption. Moreover, multiple laser pulses progressively reshape the surface; at sufficiently high fluence, this can drive phase transitions, induce surface deformation, or even remove material via spallation or evaporation. Capturing this interpulse feedback is therefore essential for an accurate description of the sample’s temporal evolution and final resolidified structure.

In this work, we present a fully coupled Maxwell-Two-Temperature Model-Molecular Dynamics (M-TTM-MD) framework in which electromagnetic field propagation, nonequi-

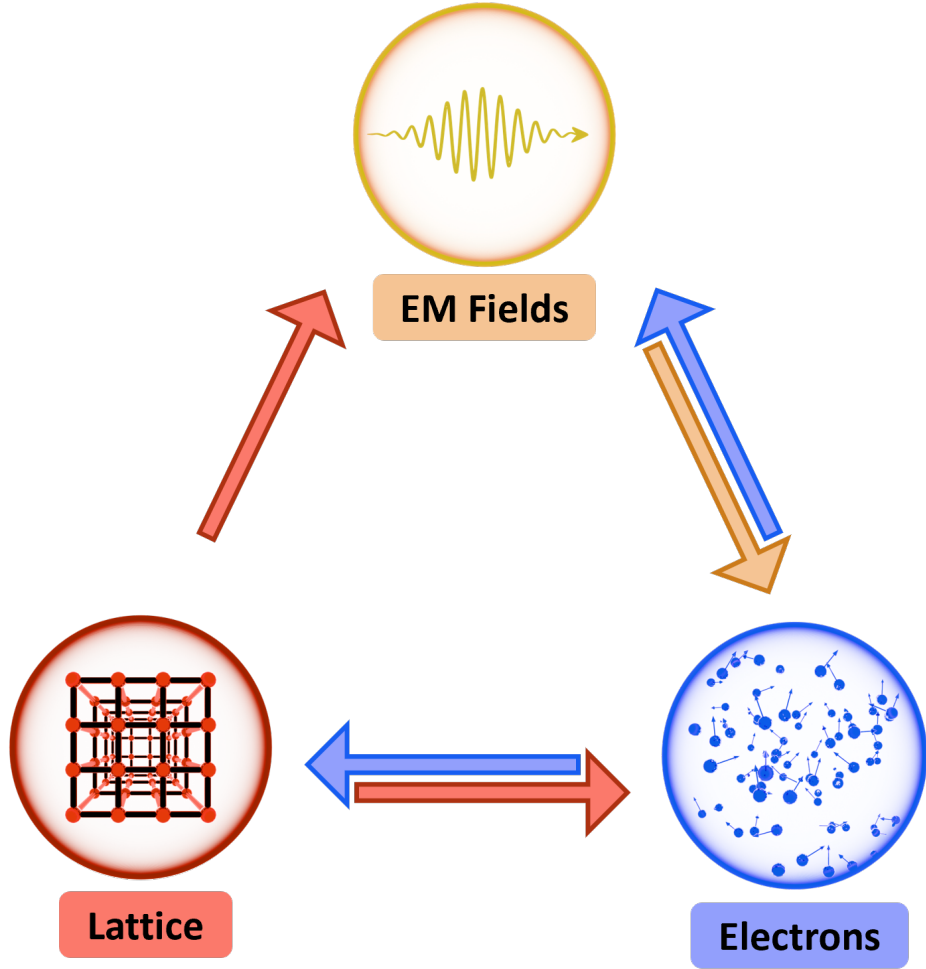


FIG. 1. Schematic representation of the different interactions accounted for in the M-TTM-MD model. The electromagnetic (EM) wave propagates through the material, where it is absorbed by the electronic subsystem, leading to a rapid increase of the electron temperature T_e . The energy is then transferred to the lattice subsystem via electron-phonon coupling, raising the lattice temperature T_l . The elevated lattice temperature induces atomic motion and structural changes, which in turn affect the material's optical properties and modify the EM wave scattering and absorption. This feedback loop continues throughout the laser–matter interaction process.

librium electron and lattice heating, and atomistic structural dynamics are treated self-consistently within a single computational model. The electromagnetic problem is solved using the Finite-Difference Time-Domain (FDTD) method [17, 18], yielding a spatially and temporally resolved field distribution from which the locally absorbed energy density is evaluated and introduced as a source term for the electronic subsystem. The different inter-

actions between the different subsystems can be summarized in Fig. 1, where the absorption of the incident EM wave rapidly elevates the electron temperature T_e , after which electron-phonon coupling transfers that energy to the lattice and raises the lattice temperature T_l on a picosecond timescale. The associated temperature elevation induces a rapid atomic motion, stress build-up, and phase transformations, thereby modifying the surface morphology. Variations in the material density as well as in the electron and lattice temperatures alter the modeled material’s optical response at the interface and, consequently, the subsequent field surface distribution and absorption. This feedback between the lattice’s thermodynamic properties (temperature, pressure and density), the electron’s thermal diffusion equation and the electromagnetic fields’ distribution forms a closed loop that ensures a self-consistent evolution of the coupled modules. The implementation targets large-scale computations through MPI-based parallelization and employs explicit energy accounting to maintain consistency across the FDTD, TTM, and MD components. The resulting framework enables quantitative, spatially resolved investigations of ultrafast energy transport and structural evolution in different materials under strongly nonequilibrium excitation.

II. THE M-TTM-MD MODEL

A. Overview of the simulation framework

As mentioned previously, the main objective of the proposed Maxwell-Two-Temperature Model-Molecular Dynamics (M-TTM-MD) is to derive, with high precision, a self-consistent source term for ultrafast laser excitation capable of interacting with metallic systems of varying geometrical complexity. The Finite-Difference Time-Domain (FDTD) method is therefore employed to calculate the electromagnetic energy absorbed by the material, where the field is discretized on a uniform Yee grid [17–20]. Each cell stores the field components and is updated at every timestep to numerically solve Maxwell’s equations. In parallel, the TTM-MD framework simulates the atomic-scale dynamics of solids under external excitation by integrating Newton’s equations of motion while ensuring local energy balance between the electronic and lattice subsystems. The integration of these two solvers requires the consistent coupling of their respective domains. The M-TTM-MD framework thus employs three spatial grids FDTD, TTM and MD. The MD (*reference mesh*) consists of the discrete atomic

positions, while the FDTD and TTM meshes are *continuum meshes* that calculate the fields and temperatures of the different subsystems respectively, while updating spatially averaged quantities such as the pressure and material density from the MD grid. The resolutions and timesteps must be chosen to ensure numerical stability and physical compatibility between all the modules. The FDTD grid is defined with uniform cell size $\Delta_x = \Delta_y = \Delta_z = \Delta_{FDTD}$, typically set equal to or smaller than the TTM cell size, $\Delta_{FDTD} \approx \Delta_{TTM}$, to ensure accurate mapping of the local electromagnetic energy flux to the electronic temperature distribution (see Fig. 2). For accurate resolution of the smallest optical wavelength λ_{\min} and fine geometrical features, Δ_{FDTD} must satisfy:

$$\Delta_{FDTD} \leq \min \left(4d_{\min}, \frac{\lambda_{\min}}{N_d} \right), \quad (1)$$

where d_{\min} is the smallest feature size and $N_d \geq 10$ denotes the number of grid cells per wavelength. When ablation or evaporation produces sub-resolution surface features that violate the inequality (1), these are neglected by the FDTD routine to maintain numerical stability. The FDTD timestep is constrained by the Courant-Friedrichs-Lowy (CFL) condition [18], yielding $t_{FDTD} \approx 10^{-3}$ fs, while the TTM loop operates with $t_{TTM} \approx 10^{-2}$ fs. A counter variable synchronizes both loops, ensuring proper temporal coupling. The FDTD subroutine runs until convergence, typically after the electromagnetic wave fully traverses the domain such that the total FDTD iterations are set to $N_{\text{step}} \geq 12\tau_{\text{las}}$, where τ_{las} is the pulse duration. The fields are then absorbed by the domain boundaries where Convolutional Perfectly Matched Layers (CPMLs) have been implemented [18, 21] to absorb any non-physical reflections into the simulation box. The coupling between the FDTD and TTM-MD solvers also incorporates the material's evolving atomic density. Cells are activated when $\rho^{\text{mat}} \geq \rho_0^{\text{mat}}/10$ and deactivated otherwise, with ρ_0^{mat} being the initial density of the material at room temperature and $\epsilon_r = 1$ denoting the relative permittivity in vacuum regions. For intermediate densities, a linear interpolation is applied: $\epsilon_r = \frac{\rho^{\text{mat}}}{\rho_{\text{init}}^{\text{mat}}} \epsilon_{\text{mat}}$. Moreover, ϵ_r evolves dynamically with both the electron temperature T_e and laser frequency ω_{las} , according to [22]. This temperature- and wavelength-dependent dielectric function is incorporated into the FDTD scheme using the well-known Auxiliary Differential Equation (ADE) method [18, 20, 23], and is updated at each FDTD timestep to capture the transient modification of the material's optical properties under laser excitation.

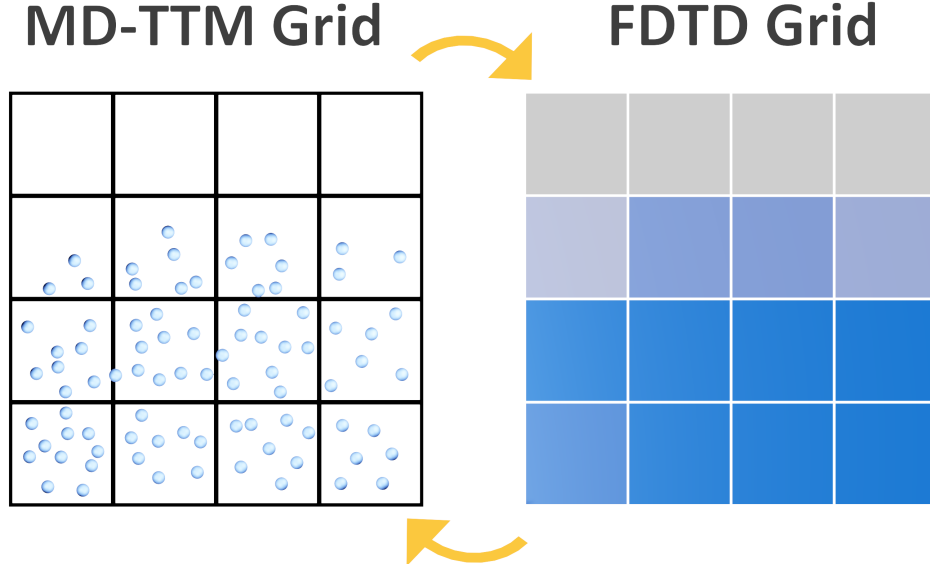


FIG. 2. Schematic representation of the relationship between the FDTD and TTM-MD continuum cells. Lower density of atoms in the MD cells, leads to decreased values in the dielectric function of the material in the FDTD approach.

The computational domain (Fig. 3) comprises several regions: the central TTM-MD zone containing the material, surrounded by the total field (TF) region and the scattered field (SF) zone, both enclosed by the CPMLs. Periodic boundary conditions are retained in the TTM-MD module to emulate an infinite lattice, while they are omitted in the FDTD solver to prevent artificial field amplification. This configuration ensures a self-consistent simulation of ultrafast energy absorption, transport, and structural response within the M-TTM-MD framework.

B. Calculating the energy absorption

Once the FDTD and TTM-MD modules are initialized with the aforementioned considerations, the M-TTM-MD algorithm enters its main loop, where all quantities—temperature distributions, interatomic forces, particle positions and velocities, and electromagnetic field components—are iteratively updated in a self-consistent manner (see Fig. 4). In this coupled cycle, the electromagnetic field drives electron heating through the FDTD source term Q_{las} which is computed from the divergence of the Poynting vector \vec{S} , representing the local

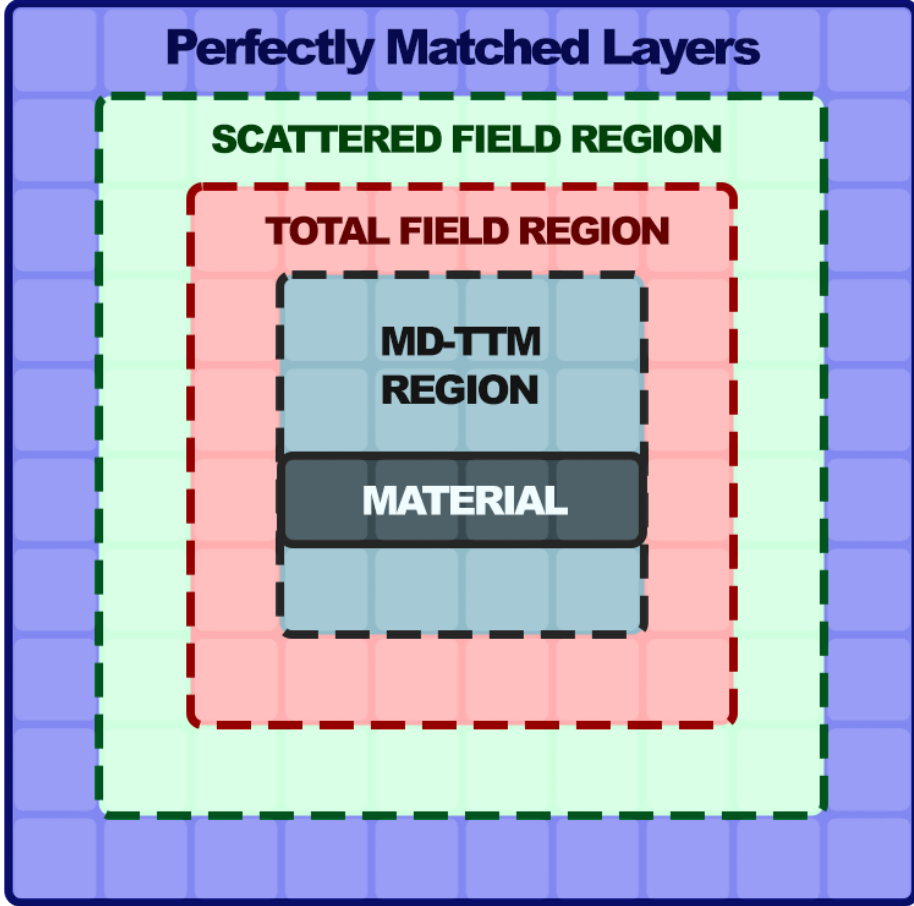


FIG. 3. Schematic representation of the computational domain used in the algorithm. The domain consists of several regions: the central TTM-MD region represents the simulated material. The surrounding total field region (red dashed border) contains the incident electromagnetic field interacting with the material, while the scattered field region (green dashed border) accounts for the outgoing scattered waves. The outermost Perfectly Matched Layers (blue shaded region) absorb outgoing waves to prevent reflections back into the simulation box.

electromagnetic energy flux penetrating the material:

$$Q_{\text{las}} = -\vec{\nabla} \cdot \vec{S} = -\vec{\nabla} \cdot (\vec{E} \times \vec{H}). \quad (2)$$

To evaluate Q_{las} on the discrete Yee grid at cell indices (i, j, k) and timestep n , the vector \vec{S} is defined as:

$$\vec{S} = \begin{pmatrix} S_x|_{i+\frac{1}{2},j,k}^n \\ S_y|_{i,j+\frac{1}{2},k}^n \\ S_z|_{i,j,k+\frac{1}{2}}^n \end{pmatrix}, \quad (3)$$

yielding the discretized form:

$$Q_{\text{las}}|_{i,j,k}^n = -\frac{S_x|_{i+\frac{1}{2},j,k}^n - S_x|_{i-\frac{1}{2},j,k}^n}{\Delta x} - \frac{S_y|_{i,j+\frac{1}{2},k}^n - S_y|_{i,j-\frac{1}{2},k}^n}{\Delta y} - \frac{S_z|_{i,j,k+\frac{1}{2}}^n - S_z|_{i,j,k-\frac{1}{2}}^n}{\Delta z}. \quad (4)$$

Each component of \vec{S} is derived from interpolated electric and magnetic field values. For example:

$$S_x|_{i+\frac{1}{2},j,k}^n = \check{E}_y|_{i+\frac{1}{2},j,k}^n \check{H}_z|_{i+\frac{1}{2},j,k}^n - \check{E}_z|_{i+\frac{1}{2},j,k}^n \check{H}_y|_{i+\frac{1}{2},j,k}^n, \quad (5)$$

where the interpolated components are obtained by simple averaging over adjacent Yee-grid points, for instance:

$$\begin{aligned} \check{E}_y|_{i+\frac{1}{2},j,k}^n &= \frac{1}{4} \left(E_y|_{i+1,j+\frac{1}{2},k}^n + E_y|_{i,j+\frac{1}{2},k}^n + E_y|_{i+1,j-\frac{1}{2},k}^n + E_y|_{i,j-\frac{1}{2},k}^n \right), \\ \check{E}_z|_{i+\frac{1}{2},j,k}^n &= \frac{1}{4} \left(E_z|_{i+1,j,k+\frac{1}{2}}^n + E_z|_{i,j,k+\frac{1}{2}}^n + E_z|_{i+1,j,k-\frac{1}{2}}^n + E_z|_{i,j,k-\frac{1}{2}}^n \right). \end{aligned}$$

The remaining components $S_y|_{i,j+\frac{1}{2},k}^n$ and $S_z|_{i,j,k+\frac{1}{2}}^n$ are computed analogously.

When the FDTD mesh is finer than the TTM grid, the latter's cell size is defined as a multiple of the FDTD spacing, $\Delta_{TTM} = m\Delta_{FDTD}$ with $m \in \mathbb{N}^*$. In this configuration, the electromagnetic flux computed at the FDTD level is volume-averaged over m^3 cells before being transferred to the corresponding TTM cell, ensuring consistent energy deposition across different resolutions. This averaging procedure maintains numerical accuracy while enabling the FDTD subroutine to resolve fine-scale optical features and the TTM module to capture spatially averaged electronic heating within the coupled M-TTM-MD framework.

C. The TTM-MD Scheme

Once the external field's source term $S(\vec{r}, t)$ is calculated, the TTM-MD module takes over the calculations. In this scheme, the energy balance is achieved by linking the TTM diffusion equation for electrons to the MD equations of motion [13]:

$$C_e(T_e) \partial_t T_e = \partial_z \left(K_e(T_e) \frac{\partial T_e}{\partial z} \right) - G(T_e - T_l) + S(\vec{r}, t), \quad (6a)$$

$$m_i \frac{\partial^2 \vec{r}_i}{\partial t^2} = \vec{F}_i + \xi m_i \vec{v}_i^T, \quad (6b)$$

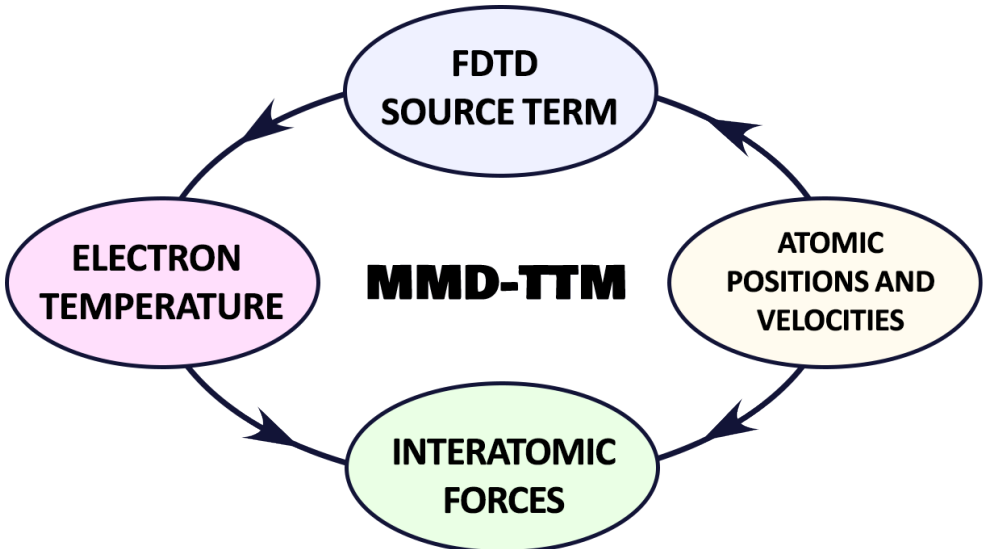


FIG. 4. Schematic illustration of the M-TTM-MD cycle, highlighting the interaction between the different subroutines. The FDTD source term drives the electron temperature elevation, influencing the lattice temperature via electron–phonon (e-ph) coupling. The increase in lattice temperature causes matter reorganization, altering the interatomic forces acting on individual particles. These forces are used to compute new positions and velocities of the particles, leading to updated atomic configurations. If the surface topology of the material changes, the scattering of the electromagnetic (EM) pulse is also affected, leading to further updates in the energy deposition profile and completing the cycle.

where the coupling factor ξ is defined as:

$$\xi = \frac{1}{n} \sum_{k=1}^n \frac{GV_N(T_e^k - T_l)}{\sum_i m_i(\vec{v}_i^T)^2}. \quad (7)$$

The coupling term distinguishes atomic thermal motion \vec{v}_i^T from the collective motion, allowing temperature-dependent energy transfer without explicit lattice heat capacity. The domain is divided into finite-difference cells where the energy exchanged over n steps is $\Delta E^{\text{e-ph}} = \sum_{k=1}^n \Delta t_{\text{FD}} GV_N(T_e^k - T_l)$, which is added to the atomic subsystem through Eq. (6b).

Lattice thermophysical properties—heat capacity, elastic constants, expansion, and melting temperature—are obtained from Embedded-Atom Method (EAM) potentials. The kinetic temperature of atoms (which is the same as the thermodynamic temperature, in equi-

librium) can be found using the equipartition theorem:

$$T_{\text{kin}} = \frac{2}{k_B(3N - N_c)} \frac{1}{2} \sum_{i=1}^N m_i v_i^2, \quad (8)$$

where N_c is the number of external constraints applied on the system and N is the total number of atoms. The pressure on the other hand is computed via the virial theorem:

$$P = \frac{Nk_B T}{V} + \frac{1}{3V} \left\langle \sum_{i=1}^N \vec{r}_i \cdot \vec{F}_i^{\text{int}} \right\rangle. \quad (9)$$

D. Algorithm of the numerical simulation

As mentioned previously, the M-TTM-MD algorithm integrates three main numerical methods: FDTD, TTM and MD simulations. To execute at scale, we employ MPI-based domain decomposition that distributes the FDTD, TTM, and MD workloads across many processes (ranks). Each rank advances its local spatial subdomain and exchanges calculated data with neighbors every timestep. The FDTD and TTM-MD modules do not necessarily use the same MPI decomposition. Therefore, quantities that are used between different modules, such as the source term for instance, are mapped back into a global array using the master rank and redivided into the different TTM-MD processors. In practice, we implement so-called *skin* layers, a few cells thick, that extend each rank's subdomain to support efficient communication across process boundaries. In the FDTD mesh, the skin layer stores \vec{E} and \vec{H} components one cell past each interface and is refreshed from neighboring ranks at every timestep, ensuring consistent curl updates at rank interfaces and continuity for CPML and TFSF boundaries [24]. In the TTM-MD module, an analogous skin region caches atoms from adjacent ranks within the neighbor cutoff; this buffer supports force evaluation near subdomain edges and anticipates atom migration. Atoms that cross a boundary are handed off to the appropriate rank at the next communication step. This design balances the computational load, reduces the memory footprint per rank, and overlaps communication with computation, thereby improving parallel efficiency and lowering the total computational time.

The general outline of the combined algorithm can be described as follows:

1. Initialize the MPI libraries and set parameters for parallelization.

2. Read the values from input files, including those for simulation parameters and field initialization.
3. Set up the MD, TTM and FDTD grid meshes and apply boundary conditions (PBC).
4. Broadcast relevant variables to all processors.
5. Initialize the FDTD method and construct its mesh based on the MD material density.
6. Start the main time loop over t_{global} :
 - (a) Run the FDTD loop until t_{FDTD} is synchronized with t_{global} :
 - i. Calculate the electromagnetic source field.
 - ii. Update the FDTD equations by calculating the new electromagnetic fields.
 - iii. Exchange data between processors as required.
 - iv. Calculate the electromagnetic energy flux.
 - v. Write FDTD variables to external files for output and potential resumption.
 - (b) Update the MD algorithm by recalculating the new forces, velocities, and atomic positions.
 - (c) Calculate the new electron and lattice temperature distributions.
 - (d) Write relevant variables to external files.
7. Once the main time loop is complete, finalize the program and close all processes.

E. Energy balance

Beyond numerical consistency, detailed energy accounting reveals how energy redistributes across subsystems during nonequilibrium processes (e.g., laser-induced melting). Accordingly, conservation is verified for each algorithmic component.

For the FDTD subroutine with a TFSF plane-wave source, we integrate the incident power and compare it with the sum of reflected/scattered and absorbed power. The incident power follows from integrating the divergence of the Poynting vector Q_{inc} at the TFSF injection cells; the scattered-field region enables a closed-surface integral of the reflected/scattered energy, and the material volume integral yields the absorbed part. Thus,

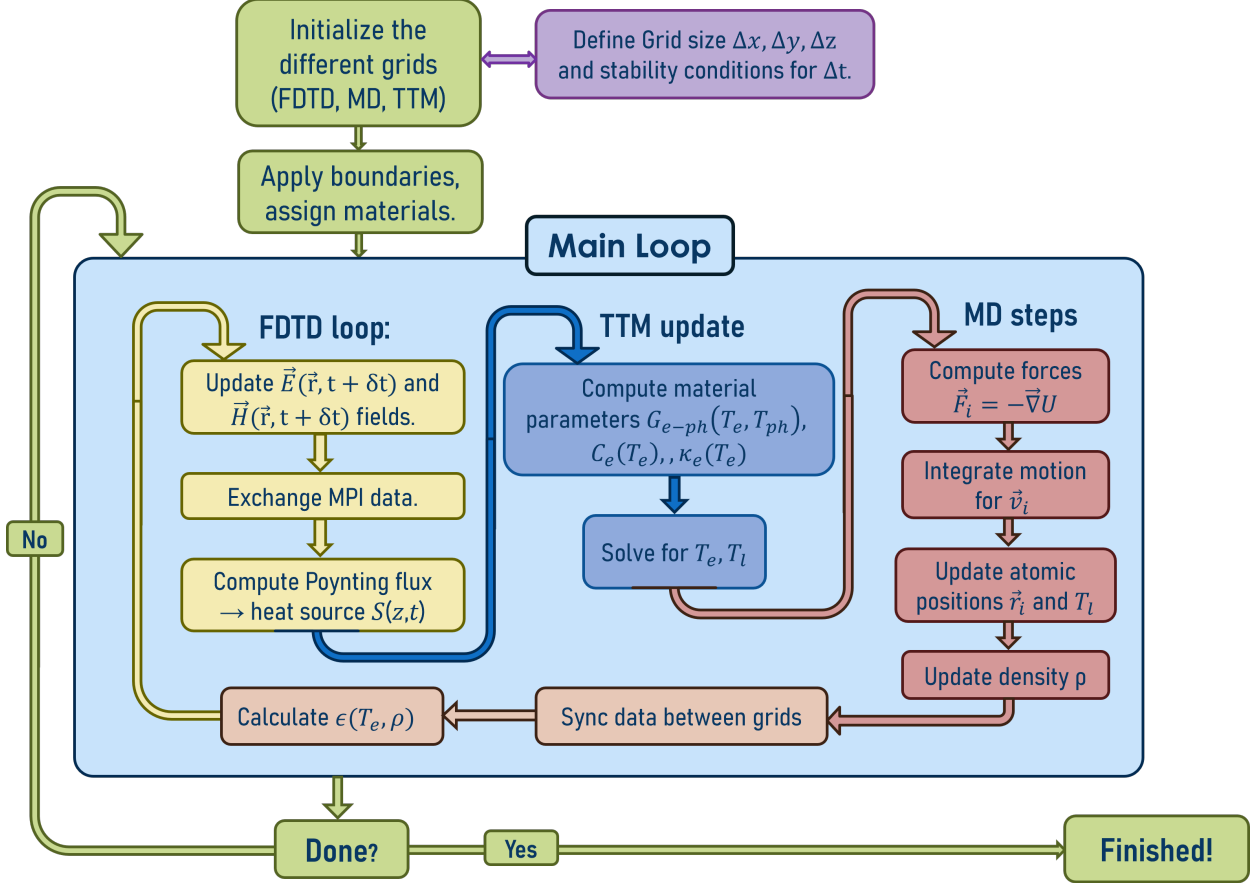


FIG. 5. Basic implementation of the M-TTM-MD algorithm. The FDTD module, the TTM energy equation, and the MD integrator exchange data at each global timestep, ensuring a self-consistent coupling between the different components.

incident = reflected/scattered + absorbed. The total electromagnetic power is calculated similarly to equation (4) within the TFSF domain $[i_0, i_1] \times [j_0, j_1] \times [k_0, k_1]$.

An alternative check integrates the electromagnetic energy-balance law in fully discrete form on the Yee grid. While Yee staggering yields accurate FDTD updates, evaluating \vec{S} , $\vec{E} \cdot \vec{J}$, and U requires timestep-wise interpolation, analogous to (4). The discrete conservation

reads:

$$\begin{aligned} \frac{\partial U}{\partial t} + \vec{\nabla} \cdot \vec{S} &= -\vec{E} \cdot \vec{J} \\ \sum_{x_i} \left(\epsilon_0 \epsilon_\infty \frac{\check{E}_{x_i}^{n+\frac{1}{2}} - \check{E}_{x_i}^{n-\frac{1}{2}}}{2\Delta t} + \frac{\check{H}_{x_i}^{n+\frac{1}{2}} - \check{H}_{x_i}^{n-\frac{1}{2}}}{2\mu_0 \Delta t} \right) + \frac{S_x|_{i+\frac{1}{2},j,k}^n - S_x|_{i-\frac{1}{2},j,k}^n}{\Delta x} \right. \\ &\quad \left. + \frac{S_y|_{i,j+\frac{1}{2},k}^n - S_y|_{i,j-\frac{1}{2},k}^n}{\Delta y} + \frac{S_z|_{i,j,k+\frac{1}{2}}^n - S_z|_{i,j,k-\frac{1}{2}}^n}{\Delta z} = - \sum_{x_i} \check{E}_{x_i}|_{i,j,k}^n \check{J}_{x_i}|_{i,j,k}^n, \quad (10) \right. \end{aligned}$$

with $x_i \in \{x, y, z\}$ and

$$\check{J}_{x_i}|_{i,j,k}^n = \check{J}_{D,x_i}|_{i,j,k}^n + \sum_{l=1}^{L_p} \check{J}_{l,x_i}|_{i,j,k}^n, \quad (11)$$

where $\check{\cdot}$ denotes interpolated quantities; e.g.,

$$\begin{aligned} \check{E}_x|_{i,j,k}^{n+\frac{1}{2}} &= \frac{1}{4} \left(E_x|_{i+\frac{1}{2},j,k}^{n+1} + E_x|_{i+\frac{1}{2},j,k}^n + E_x|_{i-\frac{1}{2},j,k}^{n+1} + E_x|_{i-\frac{1}{2},j,k}^n \right), \\ \check{H}_x|_{i,j,k}^{n+\frac{1}{2}} &= \frac{1}{4} \left(H_x|_{i,j+\frac{1}{2},k+\frac{1}{2}}^{n+\frac{1}{2}} + H_x|_{i,j+\frac{1}{2},k-\frac{1}{2}}^{n+\frac{1}{2}} + H_x|_{i,j-\frac{1}{2},k+\frac{1}{2}}^{n+\frac{1}{2}} + H_x|_{i,j-\frac{1}{2},k-\frac{1}{2}}^{n+\frac{1}{2}} \right). \end{aligned}$$

For the TTM-MD subsystem, the total system energy includes the electron energy E_e , the kinetic and potential energies from the atomic thermal motion E_a^{th} , the kinetic and potential energies emerging from the collective motion of the ions E_a^c , and melting energy E_m , where $E_m = f_L H_m$, with f_L being the liquid fraction determined by the central symmetry parameter (CSP) and H_m the latent heat of melting from internal energy curves [13, 14, 25].

III. NUMERICAL SIMULATIONS OF THIN AU FILMS

In this section, we validate the M-TTM-MD framework by simulating the irradiation of a $150 \times 600 \times 15$ nm Au thin film with six femtosecond laser pulses of 300 nm wavelength, 50 fs duration, and 0.1 J/cm^2 fluence, separated by 5 ps intervals to allow partial relaxation between successive excitations. The computational domain (Fig. 6) contains the gold film on the left side and a thin dielectric layer ($\epsilon_r = 3.5$) placed above it with a narrow vacuum gap, mimicking the Otto configuration for SPP excitation [26, 27]. The FDTD grid resolves both materials with uniform spacing in all spatial directions and using a grid size equal to that utilized in the TTM mesh. The MD algorithm on the other hand contains approximately 4×10^7 atoms in total, simulating only the Au sample and neglecting the glass material.

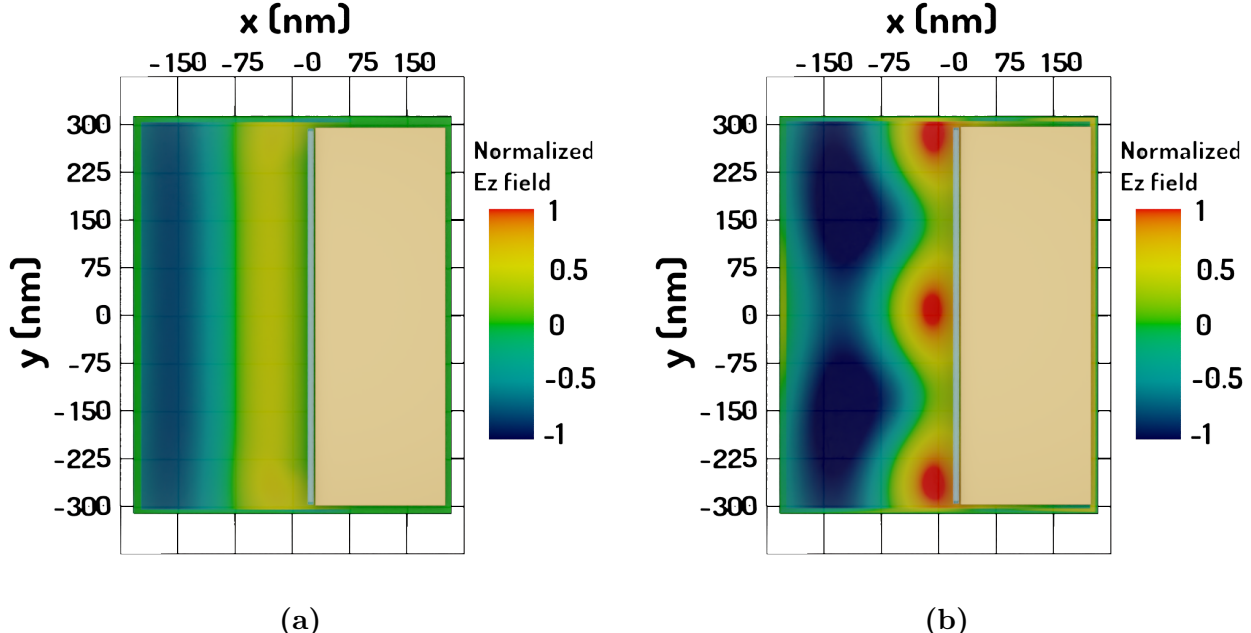


FIG. 6. Normalized electric field E_z during the FDTD run: (a) A normally incident plane wave is injected in the total-field (TF) region and impinges on the Au thin film after being transmitted from a thin glass layer mimicking the Otto configuration; (b) Interference between incident, reflected, and transmitted waves produces standing-wave fringes that set the spatial absorption profile used by the TTM module.

As shown in Fig. 6(a), a normally incident plane wave is launched into the total-field region of the FDTD domain, producing a standing-wave interference pattern through the superposition of incident, reflected, and transmitted components. This interference gives rise to a spatially modulated electric field distribution at the metal-dielectric interface, which defines the nonuniform absorption profile transferred to the TTM module. This self-consistent solution of Maxwell's equations enables the algorithm to naturally capture the actual optical absorption landscape responsible for seeding periodic energy deposition and subsequent structural modification.

During irradiation, the absorbed energy rapidly elevates the electron temperature, while the lattice remains initially cold. The electron temperature profile initially mirrors the optical absorption pattern, exhibiting high temperatures localized at the interference maxima near the surface. As energy diffuses through electron-electron collisions within a few hundred femtoseconds, these temperature gradients progressively smooth out by around one picosecond, leading to partial temperature homogenization across the film length. Similarly,

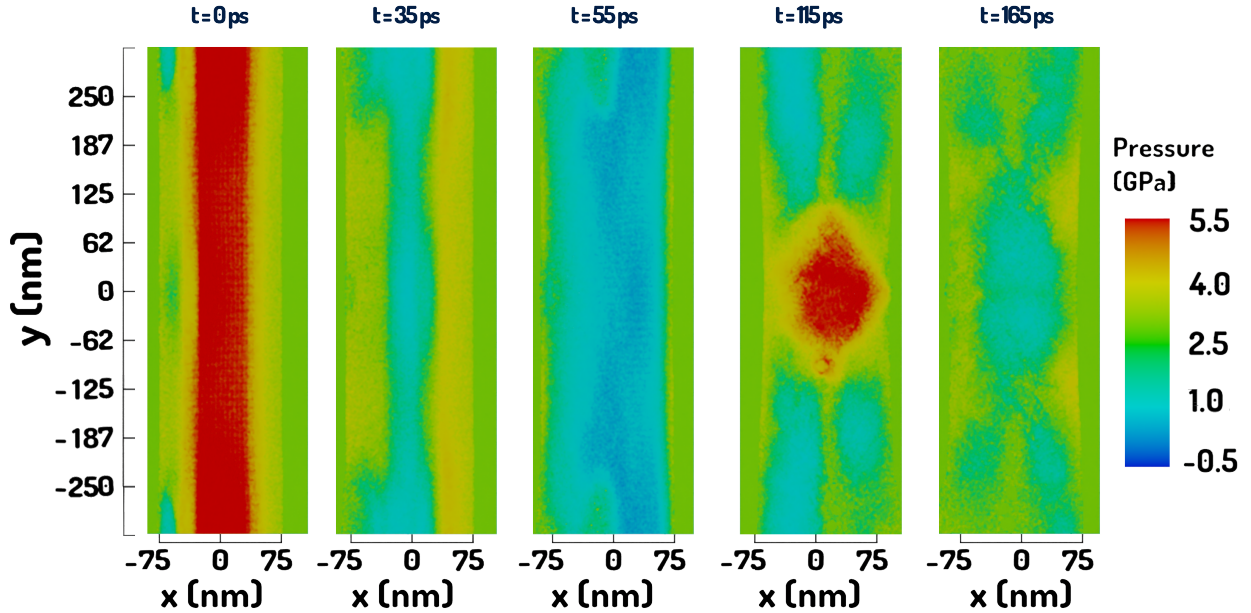


FIG. 7. Temporal evolution of the lattice pressure slices revealing stress confinement. The evolving stress field tracks the spatio-temporal energy deposition and subsequent response of the thin film.

the energy transfer to the lattice through electron-phonon coupling starts with the same spatial distribution of the surface electromagnetic fields, and progressively becomes more uniform on a picosecond timescale. Because the pulse duration (50 fs) is much shorter than the material's acoustic relaxation time, the rapid lattice heating leads to a fast build-up of internal stress confined inside the sample. The rapid thermoelastic expansion results in compressive pressures up to 6 GPa and oscillatory expansion waves that originate from the center of the film and propagate towards the free boundaries. Since in our simulations, we used periodic boundary conditions in the lateral directions normal to the incident laser pulse, the expansion waves reflect back and interfere at the center of the film as is seen in Fig. 7.

Following the spatio-temporal evolution of the lattice temperature (Fig. 8), we can see that melting initiates heterogeneously at the free surfaces, where the nucleation barrier is lowest, and subsequently propagates toward the film center as heat diffusion and acoustic oscillations continue. In the regions of strongest heating, homogeneous melting occurs simultaneously, due to the local superheating the material was exposed to, leading to liquid nucleation and facilitating phase transitions [28–30]. When the tensile phase of the stress

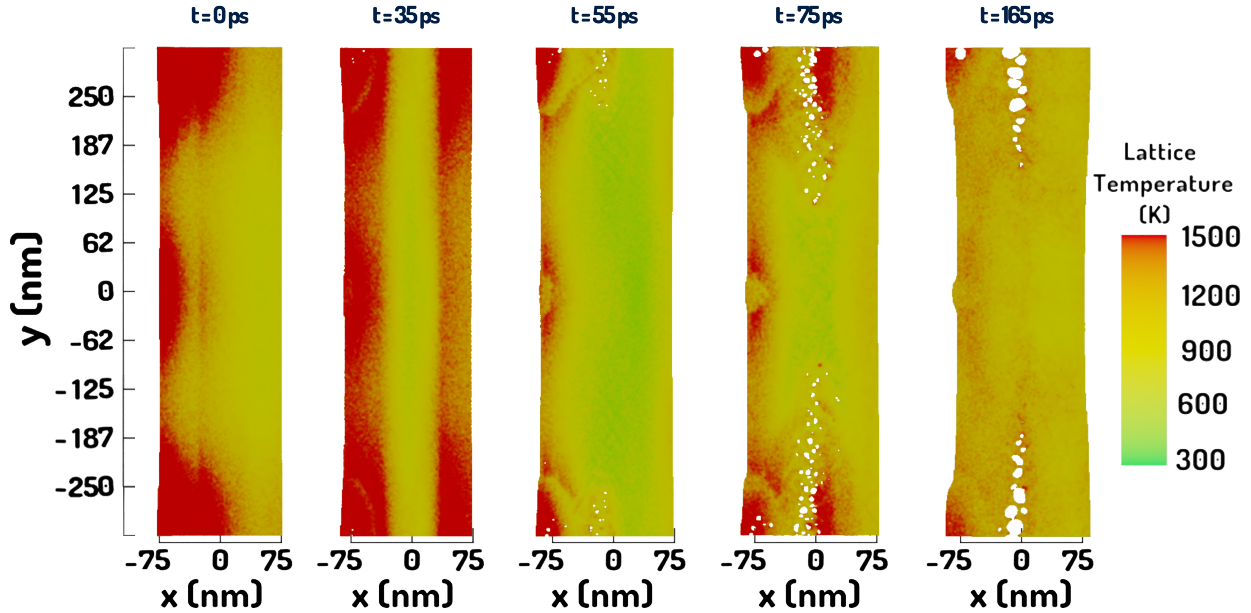


FIG. 8. Temporal evolution of the lattice temperature T_ℓ in the Au film. Heating is initially localized near the dielectric/metal interface. High pressure regions coincide with elevated temperatures.

wave traverses the molten regions, the local pressure can drop below the cavitation threshold, causing the spontaneous formation of nanoscopic voids. These voids appear preferentially at the periodic field maxima imposed by the optical interference pattern and represent a mechanical relaxation pathway within the molten layer. The expansion of these voids redistributes the surrounding melt through hydrodynamic flow, pushing material upward around the low-density regions and creating periodic surface elevations (“nanobumps”) aligned with the optical intensity peaks [13, 15].

As successive pulses arrive, partial thermal relaxation occurs but the overall temperature continues to build up, reinforcing the preexisting modulation pattern. The spatial and temporal evolution of the lattice structure (Fig. 9) displays well-defined surface protrusions accompanied by internal voids and dislocation networks that result from the large transient stresses and rapid solid-liquid transitions. The applied fluence lies in the regime where localized melting and cavitation occur without large-scale ablation or sheet detachment. Overall, the simulation captures the complete sequence of ultrafast processes, from the field-resolved optical interference, nonequilibrium electron-phonon coupling under stress confinement, transient melting and cavitation, to hydrodynamic flow leading to resolidi-

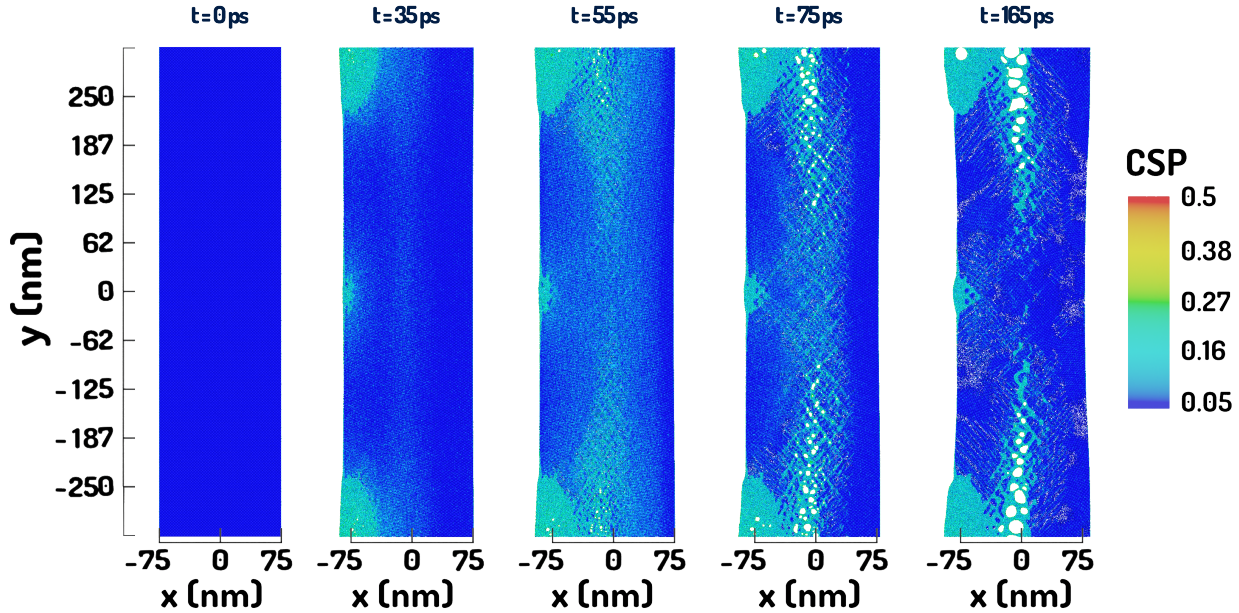


FIG. 9. Temporal evolution of the irradiated Au film where a thin slice of the full sample is plotted showcasing the atomic structure of the sample. The atoms are colored according to their local central symmetry parameter, with blue indicating crystalline order and red denoting disordered (liquid-like) states.

fied surface relief—providing a coherent microscopic picture of the initial stages of periodic surface structure formation in thin metallic films.

IV. CONCLUSIONS

We have presented a further upgrade to the TTM-MD code by integrating an FDTD solver for Maxwell's equations. The modules are coupled bidirectionally, enabling feedback between field-resolved absorption and atomistic response. By resolving the absorption landscape self-consistently and transferring it to atomistic mechanics, the model explains how femtosecond excitation seeds spatially organized morphology in metals as well as semiconductors. These results demonstrate that the framework is both predictive and physically relevant in investigations of laser-induced patterning in metals, offering deeper understanding of spatially and temporally resolved fields, temperatures, and stresses induced by external excitations.

As demonstrated, the combined M-TTM-MD method requires substantial computational resources, drawing on both TTM-MD and FDTD components to simulate intricate light-material interactions. Nonetheless, the initial simulations with the M-TTM-MD framework demonstrate promising results. While this integrated approach is able to provide insights with atomistic resolution, there is potential for optimizing the model’s efficiency. One notable improvement would be implementing a multi-resolution FDTD grid, where finer resolution is used only in critical regions (such as near the material’s surface or around dense areas with tiny geometrical features) while a coarser resolution is applied elsewhere. This approach would significantly reduce the computational load and memory usage without sacrificing the overall accuracy of the simulation.

To further enhance computational efficiency, one could explore adaptive time-stepping in both the TTM-MD and FDTD components of the algorithm since it would allow for smaller time steps only when necessary, improving the overall speed of the simulation. Alternatively, using unconditionally stable methods could remove constraints on timestep size, as discussed for FDTD techniques in [19].

This version of the code represents the first iteration of many, with the aim of developing, with the proposed enhancements, a more efficient and more versatile scheme that can be used in different fields.

DATA AVAILABILITY

The data that support the findings of this study are available from the corresponding author upon reasonable request.

AUTHOR CONTRIBUTIONS

O.B. developed the numerical framework, performed the simulations, analyzed the results, and wrote the initial manuscript draft. M.E.G. supervised the work and contributed to the interpretation of the results and to manuscript revision.

COMPETING INTERESTS

The authors declare that there is no conflict of interest.

ACKNOWLEDGMENTS

We wish to acknowledge the financial support of the Deutsche Forschungsgemeinschaft for the project GA465/15-2 as well as for the project RE1141/14-2.

- [1] M. Birnbaum, Semiconductor surface damage produced by ruby lasers, *Journal of Applied Physics* **36**, 3688 (1965).
- [2] O. Benhayoun, P. Terekhin, D. Ivanov, B. Rethfeld, and M. Garcia, Theory for heating of metals assisted by surface plasmon polaritons, *Applied Surface Science* **569**, 150427 (2021).
- [3] J. Bonse, A. Rosenfeld, and J. Krüger, On the role of surface plasmon polaritons in the formation of laser-induced periodic surface structures upon irradiation of silicon by femtosecond-laser pulses, *J. Appl. Phys* **106**, 104910 (2009).
- [4] J. Bonse and S. Gräf, Maxwell meets marangoni—a review of theories on laser-induced periodic surface structures, *Laser & Photonics Reviews* **14**, 2000215 (2020).
- [5] E. L. Gurevich, Mechanisms of femtosecond lipss formation induced by periodic surface temperature modulation, *Applied Surface Science* **374**, 56 (2016).
- [6] M. Mastellone, M. L. Pace, M. Curcio, N. Caggiano, A. De Bonis, R. Teghil, P. Dolce, D. Mollica, S. Orlando, A. Santagata, *et al.*, Lipss applied to wide bandgap semiconductors and dielectrics: Assessment and future perspectives, *Materials* **15**, 1378 (2022).
- [7] S. Schwarz, S. Rung, C. Esen, and R. Hellmann, Homogeneous low spatial frequency lipss on dielectric materials generated by beam-shaped femtosecond pulsed laser irradiation, *Journal of Laser Micro Nanoengineering* **13**, 90 (2018).
- [8] J. Sipe, J. F. Young, J. Preston, and H. Van Driel, Laser-induced periodic surface structure. i. theory, *Physical Review B* **27**, 1141 (1983).
- [9] A. Blumenstein, M. E. Garcia, B. Rethfeld, P. Simon, J. Ihlemann, and D. S. Ivanov, Formation of periodic nanoridge patterns by ultrashort single pulse uv laser irradiation of gold,

Nanomaterials **10**, 1998 (2020).

[10] P. Terekhin, O. Benhayoun, S. Weber, D. Ivanov, M. Garcia, and B. Rethfeld, Influence of surface plasmon polaritons on laser energy absorption and structuring of surfaces, *Appl. Surf. Sci.* **512**, 144420 (2020).

[11] S. Anisimov, B Rethfeld, Theory of ultrashort laser pulse interaction with a metal, P SOC PHOTHO-OPT INS **3093**, 192 (1997).

[12] N. Singh, Two-temperature model of nonequilibrium electron relaxation: A review, *Int. J. Mod. Phys. B* **24**, 1141 (2010).

[13] D. S. Ivanov and L. V. Zhigilei, Combined atomistic-continuum modeling of short-pulse laser melting and disintegration of metal films, *Physical Review B* **68**, 064114 (2003).

[14] D. S. Ivanov, T. Izgin, A. N. Maiorov, V. P. Veiko, B. Rethfeld, Y. I. Dombrovskaya, M. E. Garcia, I. N. Zavestovskaya, S. M. Klimentov, and A. V. Kabashin, Numerical investigation of ultrashort laser-ablative synthesis of metal nanoparticles in liquids using the atomistic-continuum model, *Molecules* **25**, 67 (2019).

[15] P. N. Terekhin, J. Oltmanns, A. Blumenstein, D. S. Ivanov, F. Kleinwort, M. E. Garcia, B. Rethfeld, J. Ihlemann, and P. Simon, Key role of surface plasmon polaritons in generation of periodic surface structures following single-pulse laser irradiation of a gold step edge, *Nanophotonics* **11**, 359 (2022).

[16] J. Bonse and S. Gräf, Maxwell meets marangoni—a review of theories on laser-induced periodic surface structures, *Laser Photonics Rev.* , 2000215 (2020).

[17] K. Yee, Numerical solution of initial boundary value problems involving maxwell's equations in isotropic media, *IEEE Transactions on antennas and propagation* **14**, 302 (1966).

[18] A. Taflove and S. C. Hagness, *Computational electrodynamics* (1993).

[19] M. P. Allen and D. J. Tildesley, *Computer simulation of liquids* (Oxford university press, 2017).

[20] J. B. Schneider, Understanding the finite-difference time-domain method, URL: [http://www.Eecs.Wsu.Edu/~schneidj/ufdtd/\(request data: 29.11. 2012\)](http://www.Eecs.Wsu.Edu/~schneidj/ufdtd/(request data: 29.11. 2012)) (2010).

[21] J. A. Roden and S. D. Gedney, Convolution pml (cpml): An efficient fdtd implementation of the cfs-pml for arbitrary media, *Microwave and optical technology letters* **27**, 334 (2000).

[22] P. Ndione, S. Weber, D. Gericke, and B. Rethfeld, Adaptive model for the optical properties of excited gold, *Physical Review B* **109**, 115148 (2024).

- [23] M. Okoniewski and E. Okoniewska, Drude dispersion in ade fdtd revisited, *Electronics Letters* **42**, 1 (2006).
- [24] M. F. Su, I. El-Kady, D. A. Bader, and S.-Y. Lin, A novel fdtd application featuring openmp-mpi hybrid parallelization, in *International Conference on Parallel Processing, 2004. ICPP 2004.* (IEEE, 2004) pp. 373–379.
- [25] D. Zhukhovitskii and V. Zhakhovsky, Thermodynamics and the structure of clusters in the dense au vapor from molecular dynamics simulation, *The Journal of Chemical Physics* **152** (2020).
- [26] A. Otto, Excitation of nonradiative surface plasma waves in silver by the method of frustrated total reflection, *Z. Phys. A* **216**, 398 (1968).
- [27] J. Pitarke, V. Silkin, E. Chulkov, and P. Echenique, Theory of surface plasmons and surface-plasmon polaritons, *Reports on progress in physics* **70**, 1 (2006).
- [28] B. Rethfeld, D. S. Ivanov, M. E. Garcia, and S. I. Anisimov, Modelling ultrafast laser ablation, *J. Phys. D Appl. Phys.* **50**, 10.1088/1361-6463/50/19/193001 (2017).
- [29] E. G. Gamaly, The physics of ultra-short laser interaction with solids at non-relativistic intensities, *Physics Reports* **508**, 91 (2011).
- [30] E. G. Gamaly and A. V. Rode, Physics of ultra-short laser interaction with matter: From phonon excitation to ultimate transformations, *Progress in Quantum Electronics* **37**, 215 (2013).